PAPER • **OPEN ACCESS**

Site-specific symmetry sensitivity of angle-resolved photoemission spectroscopy in layered palladium diselenide

To cite this article: M Cattelan *et al* 2021 *2D Mater.* **8** 045036

View the article online for updates and enhancements.

You may also like

- Layer-dependent band engineering of Pd dichalcogenides: a first-principles study
Liang-Ying Feng, Rovi Angelo B. Villaos, Zhi-Quan Huang et al.
- Anomalous interlayer vibrations in strongly coupled layered $PdSe_2$
Alexander A Puretzky, Akinola D Oyedele, Kai Xiao et al.
- Photoresponse of wafer-scale palladium diselenide films prepared by selenization method
Chun Hin Mak, Shenghuang Lin, Lukas Rogée et al.

This content was downloaded from IP address 147.162.53.201 on 04/04/2022 at 09:44

2D Materials

PAPER

Site-specific symmetry sensitivity of angle-resolved photoemission spectroscopy in layered palladium diselenide

M Cattelan[1], C J Sayers[2], D Wolverson[3,*] and E Carpene[4,*]

[1] Elettra Sincrotrone Trieste, SS 14, Km 163.5 AREA Sci. Pk., 34149 Trieste, Italy
[2] Dipartimento di Fisica, Politecnico di Milano, 20133 Milano, Italy
[3] Department of Physics, University of Bath, Centre for Nanoscience and Nanotechnology, Bath, BA2 7AY, United Kingdom
[4] IFN-CNR, Dipartimento di Fisica, Politecnico di Milano, 20133 Milano, Italy
[*] Authors to whom any correspondence should be addressed.

E-mail: pysdw@bath.ac.uk **and** ettore.carpene@polimi.it

Keywords: $PdSe_2$, band structure, angle-resolved photoemission spectroscopy, density functional theory

OPEN ACCESS

RECEIVED
21 July 2021

REVISED
31 August 2021

ACCEPTED FOR PUBLICATION
8 September 2021

PUBLISHED
5 October 2021

Original Content from this work may be used under the terms of the Creative Commons Attribution 4.0 licence.

Any further distribution of this work must maintain attribution to the author(s) and the title of the work, journal citation and DOI.

Abstract

Two-dimensional (2D) materials with puckered layer morphology are promising candidates for next-generation optoelectronics devices owing to their anisotropic response to external perturbations and wide band gap tunability with the number of layers. Among them, palladium diselenide ($PdSe_2$) is an emerging 2D transition-metal dichalcogenide, with a band gap ranging from $\sim$ 1.3 eV in the monolayer to a predicted semimetallic behaviour in the bulk. Here, we use angle-resolved photoemission spectroscopy to explore the electronic band structure of $PdSe_2$ with energy and momentum resolution. Our measurements reveal the semiconducting nature of the bulk. Furthermore, constant binding-energy maps of reciprocal space display a remarkable site-specific sensitivity to the atomic arrangement and its symmetry. Supported by density functional theory calculations, we ascribe this effect to the inherent orbital character of the electronic band structure. These results not only provide a deeper understanding of the electronic configuration of $PdSe_2$, but also establish additional capabilities of photoemission spectroscopy.

Transition metal dichalcogenides (TMDs) host highly attractive properties for fundamental studies of novel physical phenomena and for applications ranging from opto-electronics to sensing at the nanoscale [1, 2]. Among all TMDs, those based on noble metals (Pd, Pt) received less attention because of their high cost, until the recent discovery of a layer-controllable metal-to-semiconductor transition [3–6], which has motivated their investigation in the last few years. Similar to the extensively investigated black phosphorus [7–10], with a band gap varying from 0.3 eV in the bulk to 1.5 eV in the monolayer [11], palladium diselenide ($PdSe_2$) is characterised by an in-plane puckered structure resulting in an anisotropic response to external stimuli, such as light [12], electric field [13] and strain [14, 15]. In addition, a linear dependence of the band gap on the number of layers has been observed [3, 16]: the monolayer is predicted to have an indirect gap of 1.3 eV [17], which monotonically decreases to 0 eV as the thickness exceeds 40–50 layers, suggesting semimetallic behaviour. However, unlike black phosphorus and the majority of TMDs, which share hexagonal crystal structures, the low-symmetry pentagonal atomic arrangement of $PdSe_2$ gives rise to exotic thermoelectric, mechanical and optical properties [18–20].

Here, we investigate the electronic structure of $PdSe_2$ for the first time using angle-resolved photoemission spectroscopy (ARPES). We clarify the semiconducting nature of the bulk by direct measurements of the electronic bands in reciprocal space. Furthermore, we reveal a previously unexplored sensitivity of photoemission to the site-specific crystal symmetry. In particular, constant binding-energy cuts of the surface-projected Brillouin zone (BZ) disclose the dominant chemical/orbital character of the metal atoms in the top-most valence band (VB), while the effect of the chalcogen species becomes relevant at binding energies exceeding 1 eV. This finding is corroborated by plane wave density functional theory (DFT) calculations employing the Perdew–Burke–Ernzerhof (PBE) functional.

The crystallographic morphology of $PdSe_2$ is sketched in figure 1. Its stable configuration is

© 2021 The Author(s). Published by IOP Publishing Ltd

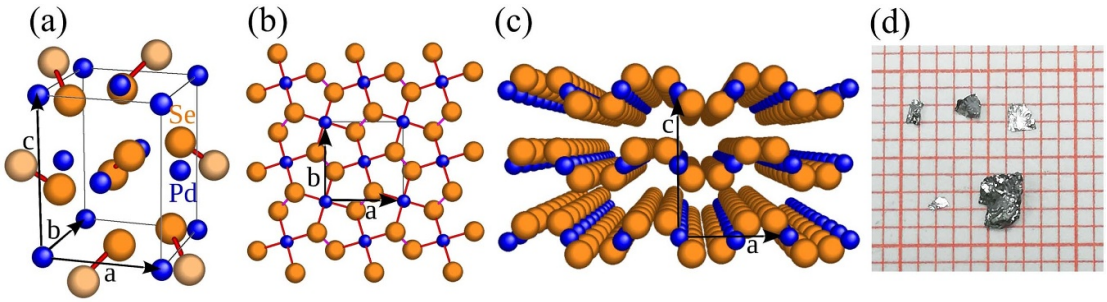

Figure 1. Unit cell (a), top (b) and side (c) views of $PdSe_2$ crystal structure. The red links in panel (a) indicate the bonds related to Se_2 dimerization. (d) Typical bulk crystals on mm-scale paper.

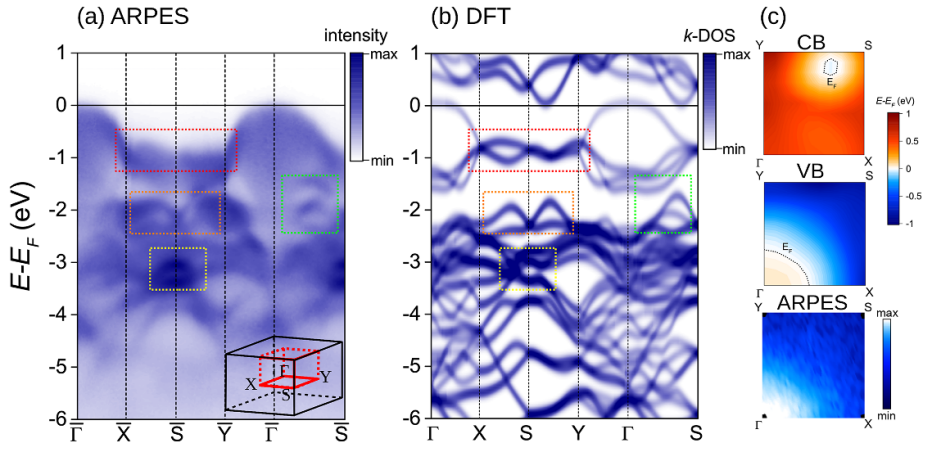

Figure 2. (a) Electronic band structure of $PdSe_2$ measured by ARPES ($h\nu = 74$ eV). The inset shows a sketch of the first BZ. (b) k-resolved DOS obtained with DFT calculations along the same path in reciprocal space used in panel (a). (c) DFT mapping of the CB (top) and VB (middle) on a 2D portion of the first BZ: dashed black lines mark the Fermi level E_F. The 2D ARPES intensity map at E_F (bottom) reveals no signature of the CB.

orthorhombic with Pbca space group (#61) and experimental lattice parameters $a = 0.575$ nm, $b = 0.587$ nm and $c = 0.77$ nm [21]; see figure 1(a). Layers are normal to the c-axis. The top view (panel (b)) shows the characteristic pentagonal atomic arrangement of the monolayer, while the side view (panel (c)) reveals its puckered structure. Each $PdSe_2$ layer is formed by three atomic planes: the Pd atoms in the middle are covalently bound to four Se atoms located on the top and bottom sub-layers. In contrast with other TMDs where the metal atom has a +4 oxidation state, $PdSe_2$ adopts the +2 oxidation [22]. This is achieved via $(Se_2)^{2-}$ dimerisation (see red links in figure 1(a)), which provides further bonding between the top and the bottom chalcogen sub-layers.

Figure 2(a) shows the measured band structure of $PdSe_2$ along selected high-symmetry directions, following the orthorhombic unit cell notation shown in the inset (see Methods for experimental details). The top of the VB is located at the centre of the BZ and is adjacent to the Fermi level E_F. The large spectral weight at the S point ($E - E_F \simeq -3$ eV) suggests the intersection of several bands.

Figure 2(b) reports the k-resolved density of states (k-DOS) obtained with DFT calculations along the same symmetry lines adopted in panel (a) (see Methods for computational details). The main features of the occupied states are reproduced with remarkable adherence to the experimental data, in particular the dispersion of the top VB and the large DOS at the S point and $E - E_F \simeq -3$ eV, which in fact hosts an intricate overlap of several electronic bands. The coloured rectangles in panels (a) and (b) highlight additional features common to both measured and calculated band structures. Note that the featureless background intensity in figure 2(a) where no states are predicted, for example between 0 and −1 eV at the Γ point, is a common feature of ARPES; secondary electrons arising from multiple scattering events will generate a 'tail' in the energy distribution curve [23]. A contribution can also arise from the non-conservation of electron momentum normal to the surface, which will be the subject of future work (see Methods section for more discussion of this point).

Turning to the nature of the band gap, it is well-known that DFT generally underestimates band gaps in semiconductors [24, 25]. In the case of $PdSe_2$, our DFT calculations predict that bulk $PdSe_2$ is marginally semimetallic but very close to semiconducting, so that more accurate calculations (using, for example,

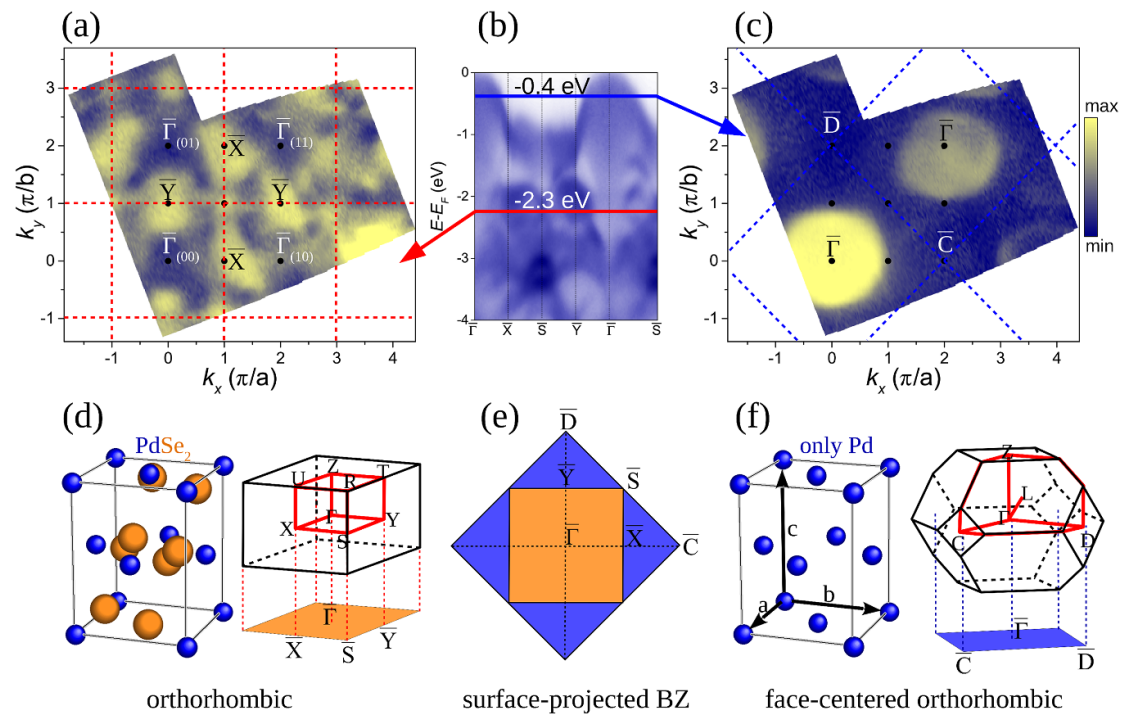

Figure 3. Constant binding-energy ARPES maps at (a) $E - E_F = -2.3$ eV and (c) $E - E_F = -0.4$ eV. Red and blue dashed lines correspond to the surface-projected orthorhombic and face-centred orthorhombic (fco) BZs, respectively (see panels d–f). (b) The selected energies are shown on the measured band structure. (d) Orthorhombic unit cell of $PdSe_2$ with the corresponding BZ. The orange-shaded area sketches the SBZ. (f) fco unit cell describing the Pd arrangement with the corresponding BZ and its surface projection (blue-shaded area). (e) Comparison of orthorhombic and fco SBZs.

the hybrid Heyd–Scuseria–Ernzerhof HSE06 density functional [26]) are essential to obtain a better estimate of the band gap; these have been reported elsewhere [27, 28] and predict bulk $PdSe_2$ to be a semiconductor. However, our DFT-D2 results (see the Methods section) still give useful insight into the locations in the BZ of the band extrema, and are reliable in terms of the VB structure (see, for example, figure S5 of Lei *et al* [28], which demonstrates that DFT-D2 and HSE06 results yield very similar topmost VBs).

The top graph in figure 2(c) shows the false-colour energy landscape of the lowest conduction band (CB) on a 2D portion of the BZ. The minimum is located close to the *YS* line (internal coordinates $[k_x, k_y] \simeq [0.33, 0.43]$ at energy $E - E_F \simeq -25$ meV). The middle graph shows the energy landscape of the highest VB, where its maximum occurs at the Γ point and energy $E - E_F \simeq +55$ meV. Hence, our calculations at the DFT level of approximation yield an overall negative gap of approximately 80 meV. In contrast to this, no evidence of electron pockets due to the CB crossing the Fermi level has been observed experimentally, as shown in the lowest graph of figure 2(c) that reports the surface-projected ARPES map at the Fermi level. In order to establish the band gap, ARPES measurements after alkali atom deposition is a possible route; the resulting shift of the VB to higher binding energy versus alkali concentration can reveal the value of the semiconducting gap. This investigation is currently in progress and will be presented separately. Thus, we conclude that $PdSe_2$ is most likely a semiconductor in the bulk (see Methods—figure 5—for additional evidence), in agreement with recent optical measurements [27, 29], although some calculations predict semimetallic behaviour [3, 17, 30]. The fact that the VB and CB are well separated in reciprocal space preserves their individual electronic features, regardless of the computed value of the band gap. In particular, the occupied states (experimentally observed by ARPES) are reproduced by DFT with remarkable accuracy.

Further insight into the electronic structure of $PdSe_2$ is achieved by inspecting the ARPES isoenergetic maps. Figure 3(a) shows the photoemission spectral weight measured on the reciprocal plane at constant energy $E - E_F = -2.3$ eV (in figure 3(b) it corresponds to the red horizontal line cutting the band structure). The horizontal and vertical axes are expressed in units of π/a and π/b, respectively. The red dashed lines identify the edges of the orthorhombic BZ. The spectral weight clearly resembles the symmetry of the BZ with peaks (yellow colour) at the $\bar{X}$ and $\bar{Y}$ points and valleys (blue colour) at $\bar{\Gamma}$. For clarity, each $\bar{\Gamma}$ point has been labelled with the corresponding in-plane Miller indices (*hk*). Figure 3(c) shows a photoemission map at $E - E_F = -0.4$ eV, i.e. closer to E_F (in figure 3(b), it corresponds to the blue horizontal line cutting the band

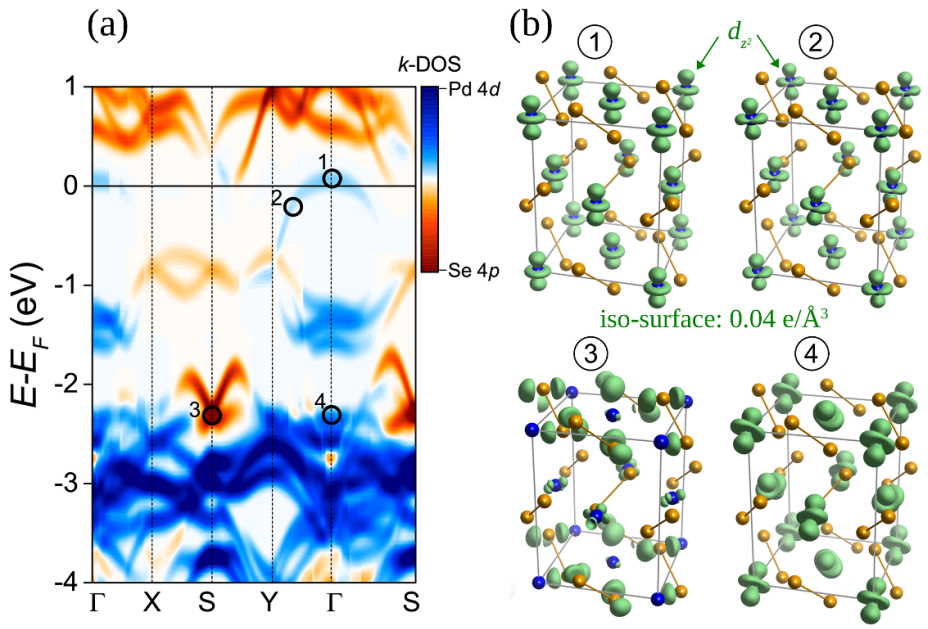

Figure 4. (a) Difference between Pd 4 *d*-projected and Se 4 *p*-projected *k*-DOS. Blue and red colour represent Pd and Se character, respectively. (b) Electron density (iso-surface value at 0.04 e Å^{-3}) at the four selected points of the band structure labelled in panel (a).

structure). The observed elliptical shapes are the surface-projected paraboloids of the top-most VB. By comparing figures 3(a) and (c), one can deduce that all $\bar{\Gamma}$ points with Miller indices satisfying the relation $h+k=odd$ are missing in panel (c). Although surprising at first glance, this observation finds a straightforward rationale by assuming a different crystal symmetry.

We will unfold this concept referring to figures 3(d)–(f). Panel (d) recalls the orthorhombic unit cell of $PdSe_2$ and the corresponding BZ. It is known that ARPES measurements of solids probe the so-called surface-projected BZ (SBZ) based on energy and momentum conservation [31]. In summary, the 3D BZ describes an infinite bulk crystal, but a true sample has surfaces. Concerning ARPES analysis, a specimen can be imagined as a semi-infinite halfspace. Such a system is characterised by a 2D (rather than 3D) translational symmetry and can be described by wave vectors k from the BZ belonging to the corresponding 2D Bravais lattice [32]. In panel (d), the SBZ is represented by the orange-shaded area. A closer inspection of the unit cell reveals that Pd atoms are arranged on a *face-centred* orthorhombic (fco) lattice, as evident in panel (f): if chalcogen atoms were absent, the corresponding first BZ would be the one sketched on the right-hand side [33] (notice the similarity with the BZ of the standard face-centred cubic lattice) [34]. Panel (e) compares the SBZs of the orthorhombic (panel (d)) and the fco (panel (f)) cells with identical lattice parameters. It can easily be verified that the following relations hold among wavevectors: $\bar{\Gamma}\bar{X}=\pi/a$, $\bar{\Gamma}\bar{Y}=\pi/b$, $\bar{\Gamma}\bar{C}=2\pi/a$, $\bar{\Gamma}\bar{D}=2\pi/b$.

Returning to the photoemission map of figure 3(c), the blue dashed lines identify the SBZ of the fco unit cell and each elliptical shape is centred at the $\bar{\Gamma}$ point of the face-centred lattice. Since Pd atoms are arranged on an fco lattice, our ARPES analysis suggests that the top-most VB originates predominantly from Pd orbitals with little contribution from Se.

In order to support this hypothesis, we have computed the orbital-projected *k*-DOS and wave functions at selected points of the band structure. Figure 4(a) reports the *difference* between Pd 4 *d*-projected and Se 4 *p*-projected *k*-DOS along the same path of the reciprocal space employed previously in figure 2 (see Methods for more details on figure 4). The blue and red colours represent the dominant Pd and Se character, respectively. The highest VB shows a strong Pd 4 *d* character with spectral weight ∼3 times larger than Se 4 *p* and marginal contributions from other atomic orbitals. On the other hand, at $E-E_F=-2.3$ eV (i.e. the same as figure 3(a)), the dominant orbital character varies with the specific position on the BZ. Here, it is of interest to visualise the wave functions in real space: figure 4(b) displays the electron density at four representative points of the band structure, labelled by circles in panel (a). The iso-surface value is taken at 0.04 e Å^{-3}. On the highest VB (labels 1 and 2), the electron density is centred on Pd atoms with d_{z^2}-like symmetry. At $E-E_F=-2.3$ eV (labels 3 and 4), the charge distribution depends on the position within the BZ: at the *S* point (label 3) it is dominated by Se 4 *p* orbitals [35], while at Γ (label 4) it is a combination of Pd 4 *d* states. These results support our hypothesis

that the same single orbital of Pd (i.e. $4d_{z^2}$) shapes the top-most VB. Recalling that Pd atoms form an fco lattice, this symmetry is retained also in reciprocal space, as revealed by our ARPES data (see figure 3(c)). A simple tight-binding approach leads to the same conclusion and is reported in the Methods section. At larger binding energies, both Pd and Se orbitals contribute to the band structure, exhibiting the standard orthorhombic symmetry of figure 3(a)).

In conclusion, we have measured the electronic band structure of bulk $PdSe_2$ by ARPES. Within the experimental accuracy, our data confirm its semiconducting nature with a minimum band gap of 50 meV (i.e. the instrumental resolution) since no evidence of CB across the Fermi level has been observed, while all electronic dispersive features below E_F are well-reproduced by our DFT calculations. Furthermore, we have demonstrated a remarkable sensitivity of the ARPES technique to site-specific symmetries of the electronic structure. This finding can be pivotal in tuning the electronic properties of $PdSe_2$-based heterostructures [36], analogous to the observed dependence of the gap on the band character of MoS_2/graphene [37, 38]. Moreover, we envisage that the chemical selectivity of ARPES allows a fine-tuning of the electronic properties. For example, the chemical substitution of metal atoms [39] will give rise to specific changes in the VB related both to doping and to modifications in the surface symmetry, to which ARPES will be sensitive. We believe that this implementation is not limited to $PdSe_2$, but it applies to a much wider class of compounds with complex crystal structures and can help clarify the subtle interactions related to correlated electronic phases, such as metal–insulator transitions, charge density waves and superconductivity [40, 41].

1. Methods

1.1. ARPES

Bulk $PdSe_2$ crystals were obtained commercially from HQ Graphene [42]. Different specimens with an average lateral size of a few mm were provided (see figure 1(d)). Samples were cleaved in an ultra-high vacuum (10^{-10} mbar) to expose a clean surface. Photoemission measurements were performed at the Spectromicroscopy beamline of the Elettra light source using 74 eV linearly polarised radiation focussed to an approximately 0.6 μm diameter spot by a Schwarzschild objective [43] and incident at 45° with respect to the sample. The energy and momentum resolution of the hemispherical electron analyser were ~50 meV and 0.03 Å^{-1}, respectively. The sample temperature was maintained at 95 K. A schematic diagram of the spatially resolved ARPES setup at Elettra and further details of the ARPES measurement have been published elsewhere [43].

1.2. DFT

The electronic band structure of $PdSe_2$ was computed with the Quantum Espresso package [44]. Exchange-correlation was considered using the PBE functional revised for solids (PBEsol). Van der Waals interactions among $PdSe_2$ layers were included using the semi-empirical Grimme's DFT-D2 correction [45]. Atoms were allowed to relax until the residual forces were below 0.0026 eV Å^{-1}. A kinetic energy cutoff energy of 60 Ry and an $8 \times 8 \times 6$ k-point mesh were used. The iso-surface rendering in figure 4(b) was performed with VESTA software [46].

1.3. Absence of CB evidence in ARPES data

Figure 5 reports three constant-energy ARPES maps of $PdSe_2$ across the Fermi level ($E - E_F = +0.5$, 0, -0.5 eV, top to bottom). Each map employs a logarithmic intensity scale ranging from 5% to 100% of the respective maximum. Even well above E_F we detected no sign of electron pockets originating from the CB, as DFT calculations would predict. Although we are not able to determine the value of the band gap with static ARPES, our data uphold the semiconducting nature of bulk $PdSe_2$.

1.4. Orbital character of the band structure (figure 4(a))

Pd 4 d and Se 4 p electrons determine the valence and conduction states of $PdSe_2$. It is instructive to 'visualise' the specific orbital character and in particular the Pd-Se *duality* along high-symmetry lines of the BZ. Here, we employ a simple colour-coded approach: the k-resolved DOS projected on Pd 4 d and Se 4 p is shown in figures 6(a) and (b), respectively. Taking the difference between the data of these two graphs, we obtain figure 4(a), where the blue and red colours encode positive (Pd) and negative (Se) values. As an example, the Pd and Se k-DOS (the latter is represented on the negative abscissa) and their difference at the Γ point are shown in figure 6(c). Note, in particular, that the Pd-projected k-DOS at the Fermi level (i.e. the VB top) is approximately three times larger than Se, as claimed in the main manuscript.

1.5. Tight-binding approach and matrix element effect

In a regular MX_6 octahedral complex (O_h symmetry) the five outer d orbitals of the transition metal M are arranged into the high-energy, double-degenerate e_g and the low-energy, triple-degenerate t_{2g} states [47], as sketched in figure 7(a). A closer look at the crystal structure of $PdSe_2$, shown in figure 7(b), reveals that each Pd is surrounded by four Se atoms belonging to the same monolayer and two apical atoms (in yellow colour) belonging to the nearest upper and lower layers. The six chalcogen atoms form an octahedron elongated along the c-axis (D_{4h} symmetry). This distortion lifts the degeneracy of the e_g states, resulting in the d_{z^2} orbital being energetically more favourable than the $d_{x^2-y^2}$ [47–49]. As we already pointed out,

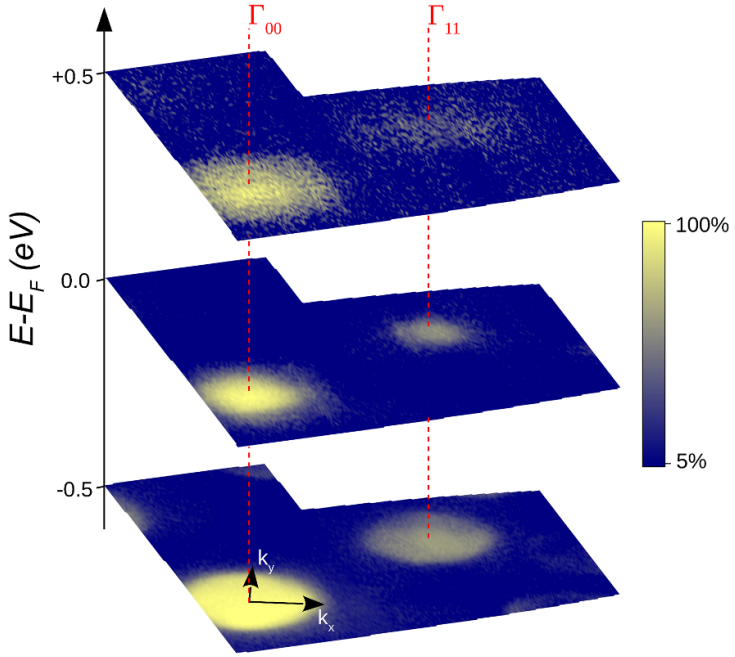

Figure 5. ARPES constant energy maps at $E - E_F = -0.5$ (bottom), 0 (middle) and +0.5 eV (top), revealing no sign of the CB.

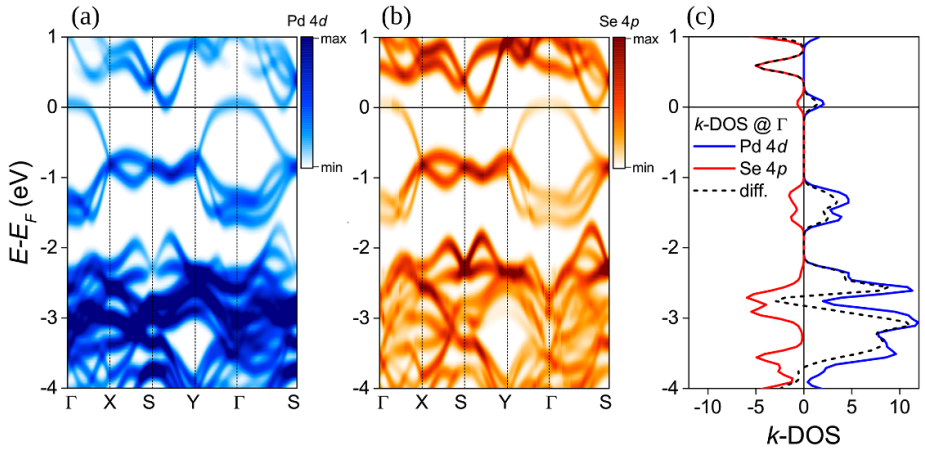

Figure 6. *k*-DOS of (a) Pd 4 *d* orbitals and (b) Se 4 *p* orbitals. (c) Comparison of Pd 4 *d* (blue) and Se 4 *p* (red) *k*-DOS at the Γ point and their difference (black dashed).

in $PdSe_2$ the oxidation state of Pd is +2 and its electronic configuration is therefore $4d^8$: six of these electrons fill the t_{2g} states completely, while the remaining two occupy the d_{z^2} orbital, leaving $d_{x^2-y^2}$ empty. d_{z^2} is therefore the highest occupied molecular orbital (HOMO) forging the top of the VB, while $d_{x^2-y^2}$ represents the lowest unoccupied molecular orbital contributing the bottom of the CB, in agreement with our own calculations (figure 4(b)) and other recent work [50].

We can now elucidate the symmetry features of the top VB observed by photoemission using a simple 2D tight-binding approach that involves only the HOMO. Metal atoms of a $PdSe_2$ monolayer are arranged on a rectangular lattice as shown in figure 8. For simplicity, we will assume a square lattice of side a. If the fco unit cell is used (panel a), a single site A is sufficient to describe the crystal. On the other hand, if the orthorhombic unit cell is assumed (panel (b)), two sites A and B must be considered: each atom $A(B)$ is surrounded by four nearest neighbours $B(A)$. In the fco case, a tight-binding approach is straightforward. Let $|R_A\rangle$ be the Wannier wave function at the specific lattice site R (i.e. the d_{z^2} orbital). The overlap integral is $\gamma = \langle R_A|U|0_A\rangle$ (U is the periodic lattice potential), where R runs over the four nearest neighbours $(+a/2, +a/2)$, $(+a/2, -a/2)$, $(-a/2, +a/2)$, $(-a/2, -a/2)$ and the eigenvalue of the Hamiltonian $\mathbb{H}$ is $E(k) = E_A + \gamma \sum_{n.n.} e^{ikR} = E_A + 4\gamma \cos(k_x a/2)\cos(k_y a/2)$, with $E_A = \langle R_A|\mathbb{H}|R_A\rangle$. Figure 8(c) shows the resulting VB dispersion along the x-axis ($k_y = 0$). If the

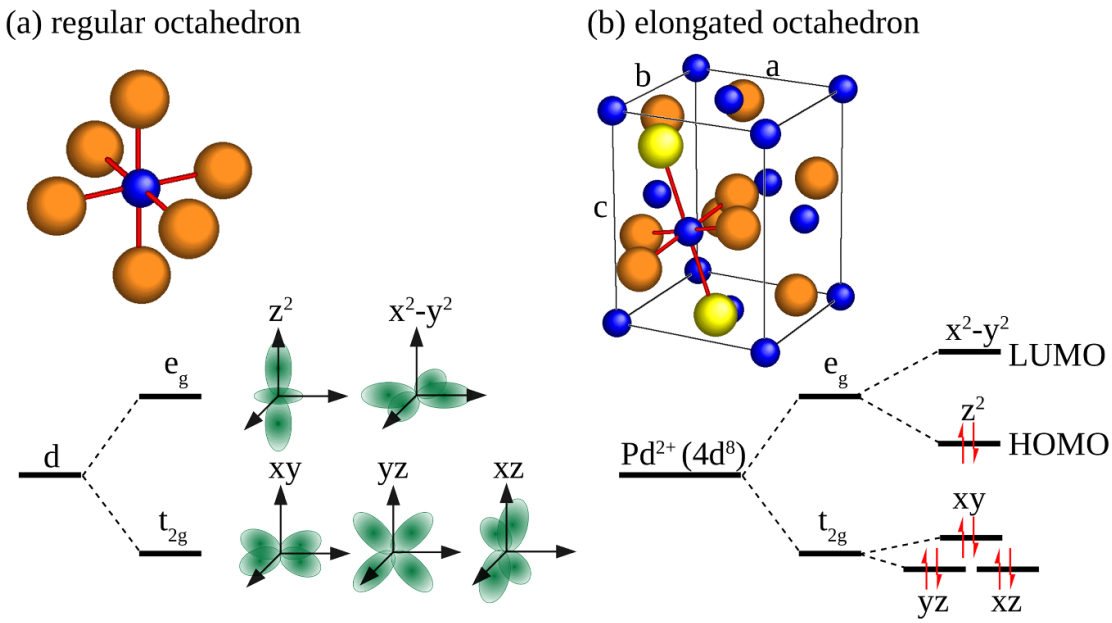

Figure 7. (a) Regular MX_6 octahedron with the corresponding crystal field splitting of d orbitals into e_g and t_{2g} states. (b) Elongated $PdSe_6$ octahedron along the c-axis: the degenerate e_g states split into HOMO and LUMO.

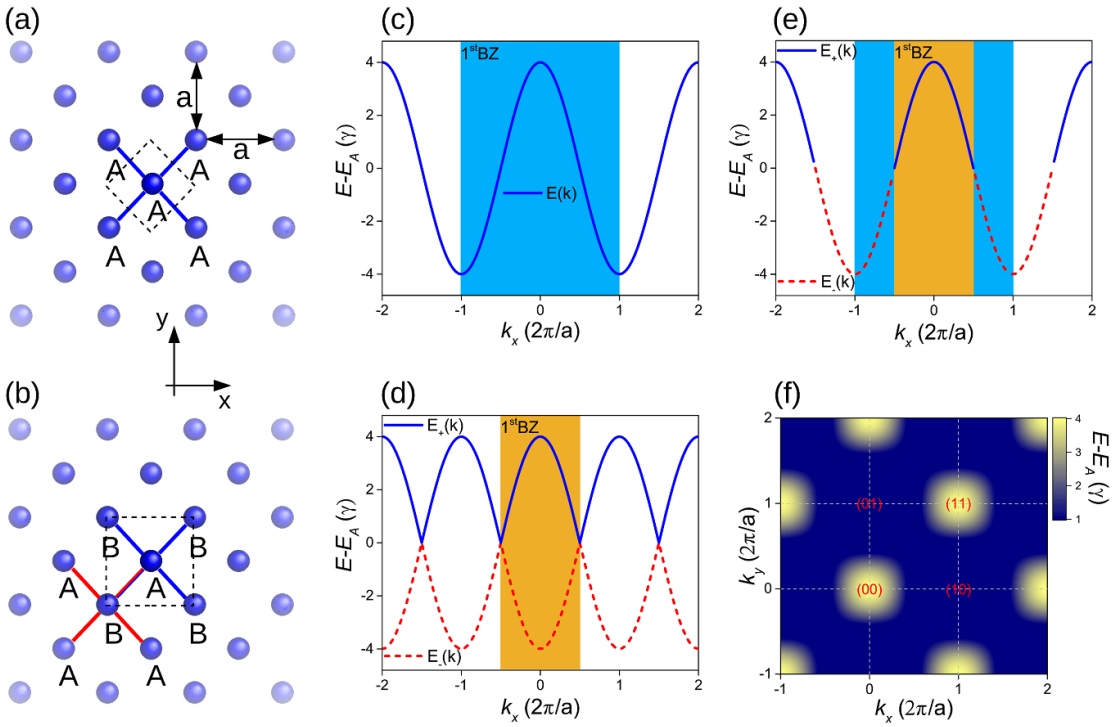

Figure 8. Pd atoms of a single $PdSe_2$ layer using (a) the fco unit cell, (b) the orthorhombic cell. Tight-binding VB dispersion employing (c) the fco cell, (d) the orthorhombic cell. (e) Equivalence of (c) and (d) after considering matrix element effect. (f) Top-VB simulation on the *xy* reciprocal plane (compare with the experimental data of figure 3(c)). The Miller indices refer to the orthorhombic cell: the missing VB peaks at (10) and (01) endorse the fco symmetry.

orthorhombic cell is used, two Wannier wave functions $|R_A\rangle$ and $|R_B\rangle$ form the basis of the tight-binding Hamiltonian:

$$\mathbb{H} = \begin{pmatrix} E_A & h \\ h^* & E_B \end{pmatrix}. \quad (1)$$

It can easily be verified that the hopping term between sites A and B is $h = 4\gamma\cos(k_x a/2)\cos(k_y a/2)$ like in the previous fco case. Since sites A and B are equivalent, it also follows that $E_A = E_B$. Thus, the two eigenvalues are $E_\pm(k) = E_A \pm |4\gamma\cos(k_x a/2)\cos(k_y a/2)|$. Figure 8(d) depicts $E_\pm(k)$ along the x-axis ($k_y = 0$). The corresponding eigenstates are $(\pm\frac{h}{|h|}, 1)$ and the

generic wave function at the lattice site R reads [51] $|R_\pm\rangle = \pm\frac{h}{|h|}e^{ikR_A}|R+R_A\rangle + e^{ikR_B}|R+R_B\rangle$. In the free electron final state approximation (here, the final state $|k_f\rangle$ is a plane wave with wave vector k_f), the photoemission matrix element $\mathbb{M}$ is expressed as the Fourier component of the tight-binding orbital $|0_\pm\rangle$ [51], i.e.

$$\mathbb{M} \propto \langle k_f|0_\pm\rangle = \langle k_f|(\pm\frac{h}{|h|}e^{ikR_A}|R_A\rangle + e^{ikR_B}|R_B\rangle) \quad (2)$$

$$= \pm\frac{h}{|h|}e^{ikR_A}\langle k_f|R_A\rangle + e^{ikR_B}\langle k_f|R_B\rangle \quad (3)$$

$$= \pm\frac{h}{|h|}e^{i(k-k_f)R_A}\langle k_f|0_A\rangle + e^{i(k-k_f)R_B}\langle k_f|0_B\rangle \quad (4)$$

which, using the momentum conservation ($k = k_f$), leads to the following photoemission intensity:

$$I_\pm \propto |\mathbb{M}|^2 \propto \left|\pm\frac{h}{|h|}\langle k_f|0_A\rangle + \langle k_f|0_B\rangle\right|^2$$
$$= \left|\langle k_f|0_A\rangle\right|^2 + \left|\langle k_f|0_B\rangle\right|^2 \pm \frac{h}{|h|}2\,\Re(\langle k_f|0_A\rangle\langle 0_B|k_f\rangle) \quad (5)$$

that simplifies to $I_\pm \propto 2\left|\langle k_f|0_A\rangle\right|^2\left(1 \pm \frac{h}{|h|}\right)$ since $|0_A\rangle = |0_B\rangle$. At this point, we notice that $\frac{h}{|h|} = \mathrm{sgn}[\cos(k_x a/2)\cos(k_y a/2)]$. Thus, $I_\pm \propto (1 \pm \mathrm{sgn}[\cos(k_x a/2)\cos(k_y a/2)]$. Referring to figure 8(d), it is easily verified that the previous equation completely suppresses the photoemission intensity of one eigenvalue $E_\pm(k)$ depending on the values of k_x and k_y. Figures 8(e) and (f) show the results: as expected, the fco band structure of figure 8(c) and the experimental data of figure 3(c) are recovered since the use of two equivalent sites is redundant and the appropriate unit cell is the fco.

We conclude with a final remark on the ARPES spectral weight of the VB at different Γ points. Comparing figures 3(c) and 8(f) it is evident how the experimental intensity of the VB at $\Gamma_{(00)}$ is the highest, while the tight-binding simulation predicts equal spectral weights for all $\Gamma_{(hk)}$ points of the fco lattice. Although ARPES at fixed photon energy is not particularly sensitive to the wave vector component k_z normal to the surface, the latter is a function of the parallel momentum [51]. When moving from $\Gamma_{(00)}$ (the real 'normal' photoemission) to $\Gamma_{(11)}$, constraints in the energy and parallel momentum conservations lead to a variation of k_z. A quantitative estimate of such variation requires the knowledge of the so-called inner potential V_0 that can be retrieved only by varying the photon energy in an ARPES experiment. In a truly 2D material this would not be an issue, since bands are k_z-independent. However, previous DFT calculations of $PdSe_2$ [17, 28] show a considerable VB dispersion along the z-axis, normal to the layer. We attribute the change in ARPES intensity of the VB vs. Miller indices to this k_z dependence. Our tight-binding simulation does not capture such an effect simply because we focussed on a 2D model to clarify the sensitivity to the specific crystal symmetry.

Data availability statement

The data that support the findings of this study are openly available at the following URL/DOI: https://doi.org/10.15125/BATH-01047.

Acknowledgments

E C acknowledges funding from the Italian PRIN Grant 2017BZPKSZ. Some of the computational work was performed at the University of Bath's High-Performance Computing Facility and support was provided by EPSRC Grants EP/G036101, EP/L015544, EP/M022188 and EP/P004830.

ORCID iDs

M Cattelan https://orcid.org/0000-0001-9314-1475
C J Sayers https://orcid.org/0000-0002-3777-5155
D Wolverson https://orcid.org/0000-0002-5578-6018
E Carpene https://orcid.org/0000-0003-3867-8178

References

[1] Manzeli S, Ovchinnikov D, Pasquier D, Yazyev O V and Kis A 2017 2D transition metal dichalcogenides *Nat. Rev. Mater.* **2** 17033
[2] Mak K F and Shan J 2016 Photonics and optoelectronics of 2D semiconductor transition metal dichalcogenides *Nat. Photonics* **10** 216–26
[3] Oyedele A D *et al* 2017 $PdSe_2$: pentagonal two-dimensional layers with high air stability for electronics *J. Am. Chem. Soc.* **139** 14090–7
[4] Miró P, Ghorbani-Asl M and Heine T 2014 Two dimensional materials beyond MoS_2: noble-transition-metal dichalcogenides *Angew. Chem. Int. Ed.* **53** 3015
[5] Wang Y *et al* 2015 Monolayer $PtSe_2$, a new semiconducting transition-metal-dichalcogenide, epitaxially grown by direct selenization of Pt *Nano Lett.* **15** 4013
[6] Ciarrocchi A, Avsar A, Ovchinnikov D and Kis A 2018 Thickness-modulated metal-to-semiconductor transformation in a transition metal dichalcogenide *Nat. Commun.* **9** 919
[7] Xia F Wang H and Jia Y 2014 Rediscovering black phosphorus as an anisotropic layered material for optoelectronics and electronics *Nat. Commun.* **5** 4458
[8] Chen P, Li N, Chen X, Ong W-J and Zhao X 2018 The rising star of 2D black phosphorus beyond graphene: synthesis, properties and electronic applications *2D Mater.* **5** 014002
[9] Gusmao R, Sofer Z and Pumera M 2017 Black phosphorus rediscovered: from bulk material to monolayers *Angew. Chem. Int. Ed.* **56** 8052

[10] Hedayat H, Ceraso A, Soavi G, Akhavan S, Cadore A, Dallera C, Cerullo G, Ferrari A C and Carpene E 2021 Non-equilibrium band broadening, gap renormalization and band inversion in black phosphorus *2D Mater.* **8** 025020

[11] Tran V, Soklaski R, Liang Y and Yang L 2014 Layer-controlled band gap and anisotropic excitons in few-layer black phosphorus *Phys. Rev.* B **89** 235319

[12] Yu J *et al* 2021 Giant nonlinear optical activity in two-dimensional palladium diselenide *Nat. Comm.* **12** 1083

[13] Di Bartolomeo A *et al* 2019 Pressure-tunable ambipolar conduction and hysteresis in thin palladium diselenide field effect transistors *Adv. Funct. Mater.* **29** 1902483

[14] Deng S, Li L and Zhang Y 2018 ACS Appl. Strain modulated electronic, mechanical and optical properties of the monolayer PdS_2, $PdSe_2$ and $PtSe_2$ for tunable devices *Nano Mater.* **1** 1932–9

[15] Luo W *et al* 2020 Anisotropic phonon response of few-layer $PdSe_2$ under uniaxial strain *Adv. Funct. Mater.* **30** 2003215

[16] Zeng L-H *et al* 2019 controlled synthesis of 2D palladium diselenide for sensitive photodetector applications *Adv. Funct. Mater.* **29** 1806878

[17] Sun M, Chou J-P, Shi L, Gao J, Hu A, Tang W and Zhang G 2018 Few-layer $PdSe_2$ sheets: promising thermoelectric materials driven by high valley convergence *ACS Omega* **3** 5971–9

[18] Pi L, Li L, Liu K, Zhang Q, Li H and Zhai T 2019 Recent progress on 2D noble-transition-metal dichalcogenides *Adv. Funct. Mater.* **29** 1904932

[19] Hassan A, Guo Y and Wang Q 2020 Performance of the pentagonal $PdSe_2$ sheet as a channel material in contact with metal surfaces and graphene *ACS Appl. Electron. Mater.* **2** 2535

[20] Lan Y-S, Chen X-R, Hu C-E, Cheng Y and Chen Q-F 2019 Penta-PdX_2 (X = S, Se, Te) monolayers: promising anisotropic thermoelectric materials *J. Mater. Chem.* A **7** 11134

[21] Gronvold R and Rost E 1957 The crystal structure of $PdSe_2$ and PdS_2 *Acta Cryst.* **10** 329

[22] Kempt R, Kuc A and Heine T 2020 Two-dimensional noble-metal chalcogenides and phospho-chalcogenides *Angew. Chem. Int. Ed.* **59** 9242

[23] Lüth H 2010 *Solild Surfaces, Interfaces and Thin Films* (Springer: Heidelberg)

[24] Perdew J P 1985 Density functional theory and the band gap problem *Int. J. Quantum Chemistry* **28** 497–523

[25] Perdew J P *et al* 2017 Understanding band gaps of solids in generalized Kohn-Sham theory *Proc. Natl Acad. Sci.* **114** 2801–6

[26] Heyd J, Scuseria G E and Ernzerhof M 2003 Hybrid functionals based on a screened Coulomb potential *J. Chem. Phys.* **118** 8207–15

[27] Lu L-S *et al* 2020 Layer-dependent and in-plane anisotropic properties of low-temperature synthesized few-layer $PdSe_2$ single crystals *ACS Nano* **14** 4963–72

[28] Lei W, Cai B, Zhou H, Heymann G, Tang X, Zhang S and Ming X 2019 Ferroelastic lattice rotation and band-gap engineering in quasi 2D layered-structure $PdSe_2$ under uniaxial stress *Nanoscale* **11** 12317–25

[29] Zhang G *et al* 2019 Optical and electrical properties of two-dimensional palladium diselenide *Appl. Phys. Lett.* **114** 253102

[30] Hamidani A, Bennecer B and Zanat K 2010 Structural and electronic properties of the pseudo-binary compounds PdX_2 (X = P, S and Se) *J. Phys. Chem. Solids* **71** 42–6

[31] Hüfner S 2003 *Photoelectron Spectroscopy* (Berlin: Springer)

[32] Bechstedt F 2003 *Principles of Surface Physics* (Heidelberg: Springer)

[33] Setyawan W and Curtarolo S 2010 High-throughput electronic band structure calculations: challenges and tools *Comput. Mater. Sci.* **49** 299–312

[34] Ashcroft N W and Mermin N D 1976 *Solid State Physics* (Philadelphia, USA: Saunders College)

[35] Point 3 in figure 4(a) is four-fold degenerate. Here we show the iso-surface of one of the bands, the others differing only by 4 *p* orbital orientation and/or Se atom.

[36] Li E *et al* 2018 Construction of bilayer $PdSe_2$ on epitaxial graphene *Nano Res.* **11** 5858–65

[37] Diaz H C, Avila J, Chen C, Addou R, Asensio M C and Batzill M 2015 Direct observation of interlayer hybridization and dirac relativistic carriers in graphene/MoS_2 van der Waals heterostructures *Nano Lett.* **15** 1135–40

[38] Pierucci D *et al* 2016 Band alignment and minigaps in monolayer MoS_2-graphene van der Waals heterostructures *Nano Lett.* **16** 4054–61

[39] Gao J *et al* 2016 Transition-metal substitution doping in synthetic atomically thin semiconductors *Adv. Mater.* **28** 9735–43

[40] Hedayat H *et al* 2019 Excitonic and lattice contributions to the charge density wave in 1*T*-$TiSe_2$ revealed by a phonon bottleneck *Phys. Rev. Research* **1** 023029

[41] Sayers C J *et al* 2020 Coherent phonons and the interplay between charge density wave and Mott phases in 1*T*-$TaSe_2$ *Phys. Rev.* B **102** 161105

[42] http://www.hqgraphene.com

[43] Dudin P, Lacovig P, Fava C, Nicolini E, Bianco A, Cautero G and Barinov A 2010 Angle-resolved photoemission spectroscopy and imaging with a submicrometre probe at the SPECTROMICROSCOPY-3.2L beamline of Elettra *J. Synchrotron Radiat.* **17** 445–50

[44] Giannozzi P *et al* 2017 Advanced capabilities for materials modelling with quantum ESPRESSO *J. Phys.: Condens. Matter* **29** 465901

[45] Grimme S, Antony J, Ehrlich S and Krieg H 2010 A consistent and accurate ab initio parametrization of density functional dispersion correction (DFT-D) for the 94 elements H-Pu *J. Chem. Phys.* **132** 154104

[46] Momma K and Izumi F 2011 VESTA 3 for three-dimensional visualization of crystal, volumetric and morphology data. J *Appl. Crystallogr.* **44** 1272–6

[47] Bersuker I B 2010 *Electronic Structure and Properties of Transition Metal Compounds: Introduction to the Theory* (Hoboken, NJ: Wiley)

[48] If ligands with apical atoms are negligible, *d* orbitals split into the square planar coordination where d_{xy} has higher energy than d_{z^2} (and the former becomes the HOMO), see [47].

[49] Soulard C, Rocquefelte X, Petit P-E, Evain M, Jobic S, Itié J-P, Munsch P, Koo H-J and Whangbo M-H 2004 Experimental and theoretical investigation on the relative stability of the PdS_2- and pyrite-type structures of $PdSe_2$ *Inorg. Chem.* **43** 1943

[50] Lei W, Wang W, Ming X, Zhang S, Tang G, Zheng X, Li H and Autieri C 2020 Structural transition, metallization and superconductivity in quasi-two dimensional layered PdS_2 under compression *Phys. Rev.* B **101** 205149

[51] Moser S 2017 An experimentalist's guide to the matrix element in angle resolved photoemission *J. Electron Spectrosc. Relat. Phenom.* **214** 29–52